Labuta *et al. Earth, Planets and Space* (2023) 75:80
https://doi.org/10.1186/s40623-023-01822-7

Earth, Planets and Space

FULL PAPER

Open Access

Modelling the seismic response of the Mýtina maar volcanic structure

Martin Labuta[1,2*], Ivo Oprsal[1,3] and Jan Burjánek[1]

Abstract

In this study, we determine the properties of the maar volcanic structure using ambient vibration analysis. We performed several ambient vibrations surveys at Mýtina maar (West-Bohemia, Czechia) to map amplification by site-to-reference spectral ratios and to estimate average shear wave velocities by array methods. As the maar diatreme is formed by a deep concave body of broken rock, strong 3D resonances develop. The site-to-reference amplification factors reach a value of 20 in the central part of the maar. Using the noise data, we demonstrate possibility of mapping the lateral dimensions of the maar infills by ambient noise measurements. To understand these observations, we developed a simplified 3D viscoelastic velocity model and simulated synthetic ambient vibrations by the finite difference method. The simulated response fitted both, measured fundamental frequencies and the amplification levels. The maximum depth of the crater was estimated to be at least 800 m.

Keywords Ambient vibrations, Site effects, 3D resonance, Spectral analysis, 3D numerical modelling, Maar volcanic structure response, Array measurements, Dispersion curves, F–K analysis

Graphical Abstract

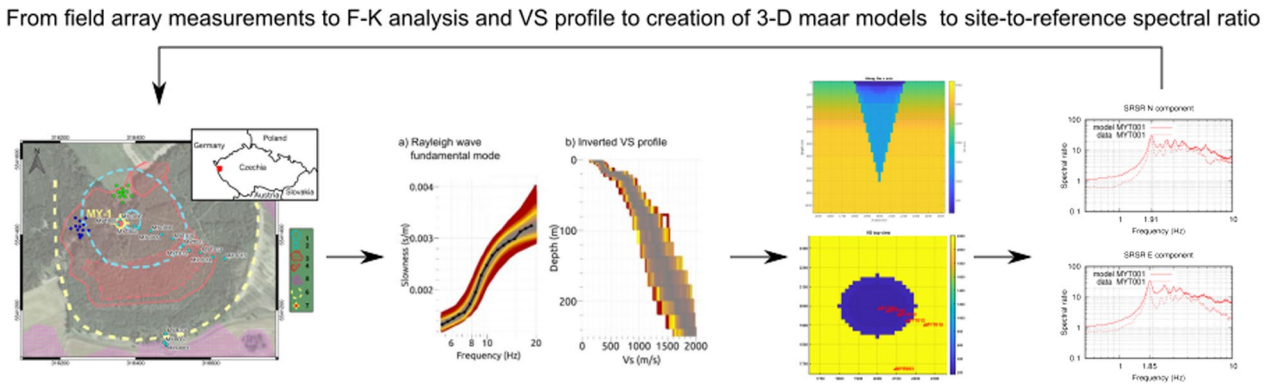

*Correspondence:
Martin Labuta
labuta@ig.cas.cz
Full list of author information is available at the end of the article

Introduction

Maar is a broad, low-relief volcanic crater, caused by a phreatomagmatic eruption. It is filled with volcanic eruption breccia, lava and sediments, and often housing a shallow lake on top (so-called maar lake). A dry maar results when the maar lake dries out, for example, due to the deposition of sediments. The Mýtina dry maar belongs to a series of recently discovered Quaternary volcanic structures in Czechia (Mrlina et al. 2009). It is situated in West Bohemia, 1 km north of the Železná hůrka Quaternary volcano, and 10 km SE from the city of Cheb, Czechia. It is the first Quaternary maar discovered in Central Europe north of the Alps and east of Volcanic Eifel (Mrlina et al. 2007).

Included in the past and up-to-date are borehole drilling and logging of the core, gravimetric, magnetic prospecting, electric resistivity tomography (ERT) and shallow seismic tomography (SST) (Mrlina et al. 2007; 2009; Flechsig et al. 2015). The gravimetric survey and modelling suggests a structure with near-surface sedimentary cover, low-density volcanic material in the shallow depth and higher density volcanic breccia in the lower part of the maar (Mrlina et al. 2009). The magnetic survey shows small circular peaks of increased magnetic intensity on the north and south edges of the maar as well as in the Železná hůrka volcano. Between these two volcanic structures, there is a zone of linearly elongated profiles of increased magnetic intensity oriented in the direction of the Tachov fault zone (TFZ) (NW–SE) (Flechsig et al. 2015). Flechsig et al. (2015) also conducted the ERT and SST, reaching modelled depths of circa 150 and 80 m, respectively. The ERT results exhibit a lower-resistivity layer in the first 100 m of depth which confirms the lithological results from borehole drilling (Mrlina et al. 2009).

The above methods determined the lateral dimensions of the studied structure but did not determine the depth of the crater, since they reached only down to the shallow subsurface (Mrlina et al. 2007; 2009; Flechsig et al. 2015). Therefore, in this study, we try to evaluate the dimensions of the maar structure and its sedimentary and volcanic fills by modelling the seismic ambient vibrations generated outside of the maar. The amplification of ground motions inside the maar body are simulated by a technique described in Burjánek et al. (2019). Due to efficient acquisition of ambient vibrations, their use has become increasingly attractive in studies on local site effects. However, the interpretations of recordings are usually based on layered media assumption. In this study, the synthetic ambient vibrations are generated using a finite-difference method for generally heterogeneous 3D media. The synthetics are processed in the same way as measurements and are compared to observed results from the ambient vibration survey. To test the different depths of the maar, we propose multiple material models consisting of P-wave and S-wave seismic velocities of conical and cylindrical shapes with various dimensions.

Methods

The frequency–wavenumber array analysis method

The frequency–wavenumber (F–K) method, which was used in this study, was developed by Capon (1969), and improved in the Geopsy software by Wathelet et al. (2020) to a high-resolution three-component F–K analysis (Wathelet et al. 2018). The seismogram is split into individual partially overlapping windows in the time domain, for which then the F–K spectra are calculated and averaged. The local spectral maxima representing the incoming waves of specific azimuth and phase velocity are then processed for each discrete frequency step within the investigated frequency range given by the geometry of the seismic stations array on surface. The minimum wavenumber resolution is controlled by the maximum distance between the neighbouring array stations (e.g. Wathelet et al. 2008). Meanwhile, the maximum resolved wavenumber relates to the minimum distance between the array stations. The considered seismic ambient noise is assumed (e.g. Bonnefoy et al. 2006) to consist mainly of surface waves, the vertical and radial components can be used to determine phase velocities of Rayleigh waves. Similarly, the transversal component can then be used to analyse Love waves. The surface waves' phase velocities are frequency dependent and the relation between the phase velocity and frequency is given by dispersion curves. We estimated the dispersion curves from array recordings using the Geopsy software (Wathelet et al. 2020), Wavedec (Maranò et al. 2012; 2017) and ArrayTools3C (Poggi and Fäh 2010) to verify the integrity of the obtained dispersion curves of the Rayleigh and Love waves.

The inversion for the seismic velocity profiles

We used the dispersion curves to invert the seismic velocity profiles in Dinver module (part of Geopsy software). We assumed 1D layered media with a fixed density of 2.2 g/cm^3 (Mrlina et al. 2007), and increasing velocities with depth. Therefore, we set our parametrization as a multi-layered model with variable thickness starting at 2.5 m at the surface and ending at 20 m at 200 m depth. For each layer, we set its possible velocity range and apply a constraint of the above-mentioned increasing seismic velocity with depth. The software then randomly generates a given number of models which fit the input

criteria. The synthetic dispersion curves are computed and compared with the observed dispersion curves, followed by optimisation of the final model selection by the neighbourhood algorithm (Sambridge 1999; Wathelet 2008), searching for the models within the given misfit range.

The site-to-reference spectral ratio (SRSR)

To determine the resonance frequency and the amplification ratio of the studied local effects of the maar, we used the site-to-reference spectral ratio computed from ambient vibrations. The SRSR method was originally introduced for analysis of earthquake recordings (Borcherdt 1970); nevertheless, SRSR calculated using noise recordings can still be representative of local site conditions (e.g. Irikura and Kawanaka 1980; Pischiutta et al. 2017; Kleinbrod et al. 2017). At least two simultaneous noise recordings were required, one located in the studied area and the second one (reference) in a near vicinity placed on the outcropping bedrock. Thus, we can determine the local site effect of the maar by eliminating source directivity and path effects by dividing the Fourier spectrum of each component of the station inside the maar by the spectrum of the corresponding component at the reference station outside. The Fourier spectra are determined by the multitaper method (Prieto et al. 2009). Assuming the seismic noise sources are all directional and randomly distributed in time and space (e.g. Bonnefoy et al. 2006), the source and path effects are the same for stations located far away from the noise sources. Since we conducted the measurement in a secluded location, we did not see any effect of a nearby directional man-made source.

Ambient vibration simulations

Numerical simulations of ambient vibrations follow a two-step procedure based on generating Green's functions and the subsequent assembly of the noise time series for a given source distribution (Burjánek et al. 2019). In the first step, Green's functions are estimated using the reciprocity method by swapping the position of the source and the receiver (e.g. Eisner and Clayton 2001). In this way, it is possible to reduce the number of numerical simulations to three times the number of receivers using three orthogonal point forces at the receiver locations to obtain a response from an arbitrary number of sources. In the second step, the synthetic noise time histories are generated by summation of responses to randomly distributed point-force sources, convolved with randomised source time functions. The details of the procedure can be found in Burjánek et al. (2019). For the numerical calculations of Green's functions, we used a finite difference method implemented in the SW4 code of Petterson and Sjögreen (2017). It can simulate seismic wave generation and propagation through a 3D inhomogeneous viscoelastic medium. The elastodynamic equations are approximated by the fourth order of accuracy in space using a grid-node-based finite difference approach, and by explicit time formulation. The SW4 also utilises a curvilinear grid below topography and grid refinements allowing smaller grid spacing at the surface. The time step is calculated automatically based on the grid spacing, the computed frequencies, and local Vs velocities. The quality factors Qp and Qs are realised by viscoelastic modelling using three standard linear solid mechanisms providing correct damping for the frequency band of interest (0.5–10 Hz).

Field experiments

Ambient vibration data used in this study were collected using Lennartz LE-3Dlite MkIII seismometers, which are three-component short-period devices with a flat response of 1 to 100 Hz. For the digitisation and recording of measurements, we used A/D converters with a bit depth of 31 bits per sample. The positions of the sensors were measured using an accurate differential GPS (DGPS) receiver that provides 1 cm precision. The seismometers were placed on customised tripods, which allowed a comfortable setting (both for levelling and orientation). Whenever possible, sensors were placed in shallow pits of ~ 20 cm to achieve better coupling with the ground, by removing the most unconsolidated soil layer, and to provide more protection against wind gusts.

We have deployed the seismic arrays at two locations to estimate the shear wave velocity structure of the crater infills (Fig. 1). The centre of the first array was 90 m north of the borehole and the centre of the second one was 110 m west of the MY-1 borehole. The borehole log shows only the lacustrine sediments within its whole depth of 80 m. The sediments comprised interbedded sand, clay and silt layers (Mrlina et al. 2009). The aim of the first array (Array 1) was to estimate the shear wave velocity of the maar's lacustrine sediments. It consisted of a station in the centre, three stations 5.5 m from the centre and 120 degrees apart creating a triangle, and two pentagons rotated by 36 degrees to each other and with diameters of 25 and 50 m, respectively. The stations were positioned in the vertices of these geometrical shapes, 14 stations were used in total. The aim of the second array (Array 2) was to estimate the shear wave velocity of volcanic breccia. The geometry of Array 2 followed the geometry of Array 1, except for the smallest 5-m triangle, which was at the southern vertex of the large 50 m pentagon, due to dense vegetation in the central part of Array 2. Moreover, ambient

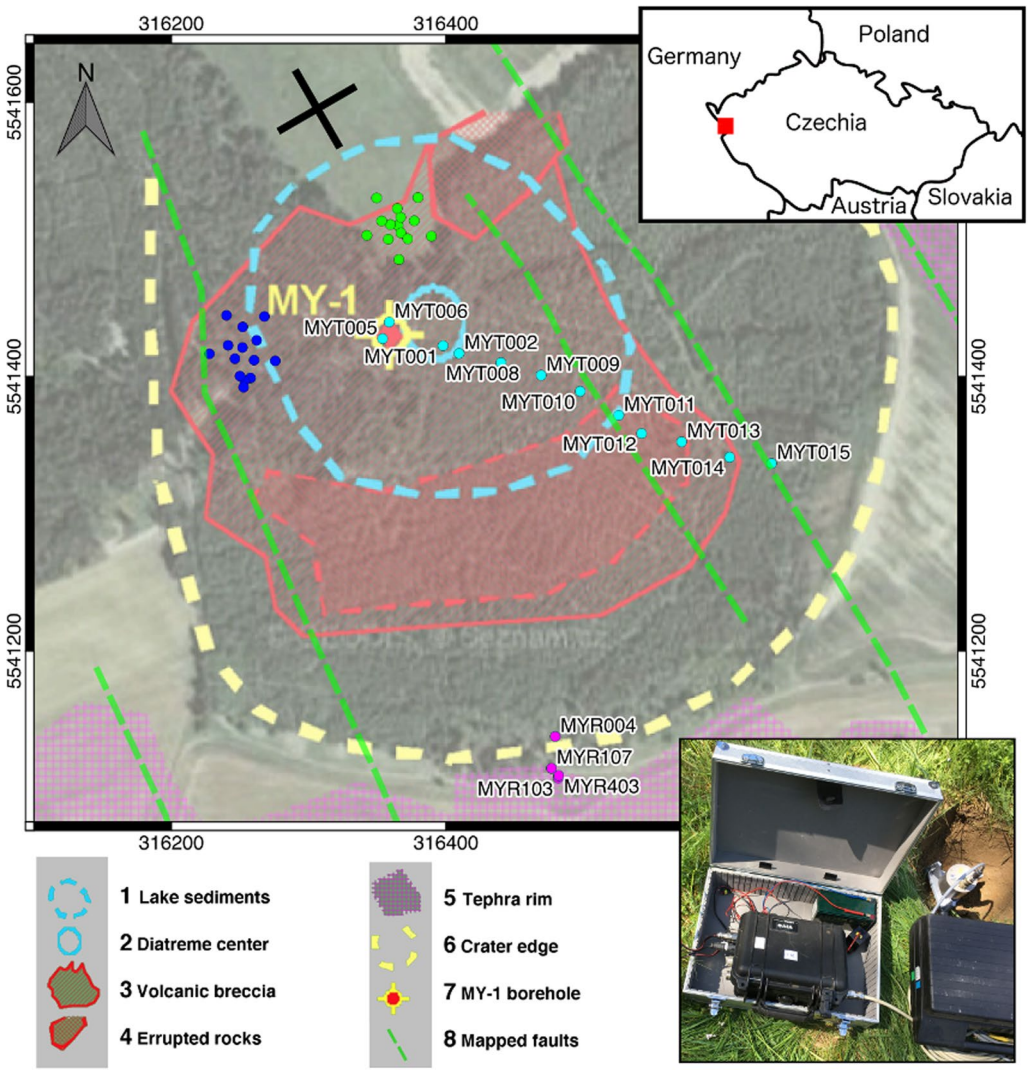

Fig. 1 An overview map of the researched area showing the positions of the seismic sensors (dots) and mapped maar features (modified after Mrlina et al. 2009). Two array configurations are shown (green dots: Array 1—lacustrine sediments; blue dots: Array 2—volcanic breccia). Maar features as presented by Mrlina et al. (2009): (1) approximate contour of the lacustrine sediments; (2) centre of maar diatreme; (3) volcanic breccia; (4) erupted magnetic rocks accumulations; (5) relicts of tephra rim outside the crater; (6) morphological edge of the crater; (7) MY-1 borehole; (8) mapped faults of the Tachov fault zone (Flechsig et al. 2015). The positions of the consecutive double-station measurements are indicated by cyan dots. The positions of the reference stations at the southern edge of the crater are shown by purple dots. The black solid cross indicates the two dominant directions of the resonance (discussed later in the results section). The coordinates are given in m of WGS84 UTM projection in the 33N zone. The inset map (top right) displays the position of the Mýtina maar (red square) in a regional context, whilst the inset photo (bottom right) shows the typical field installation

vibrations were recorded along a profile, to map seismic response from the centre to the border of the diatreme infills (Fig. 1). A reference station was always placed at the southern edge of the crater. The measurements were performed in three different time periods and several reference positions were tested (MYR104, MYR007, MYR003), with no significant differences in the recordings. The country bedrock consists of competent phyllites, quartz phyllites, and quartz lenses with mica schists (Fiala and Vejnar 1997; Tonica et al. 1998). The H/V spectral ratio calculated for the reference station did not show any peak through the studied frequency range from 0.5 to 10 Hz (see Additional file 1: Fig. S1). At least 1 h of continuous records was obtained for each of the setups.

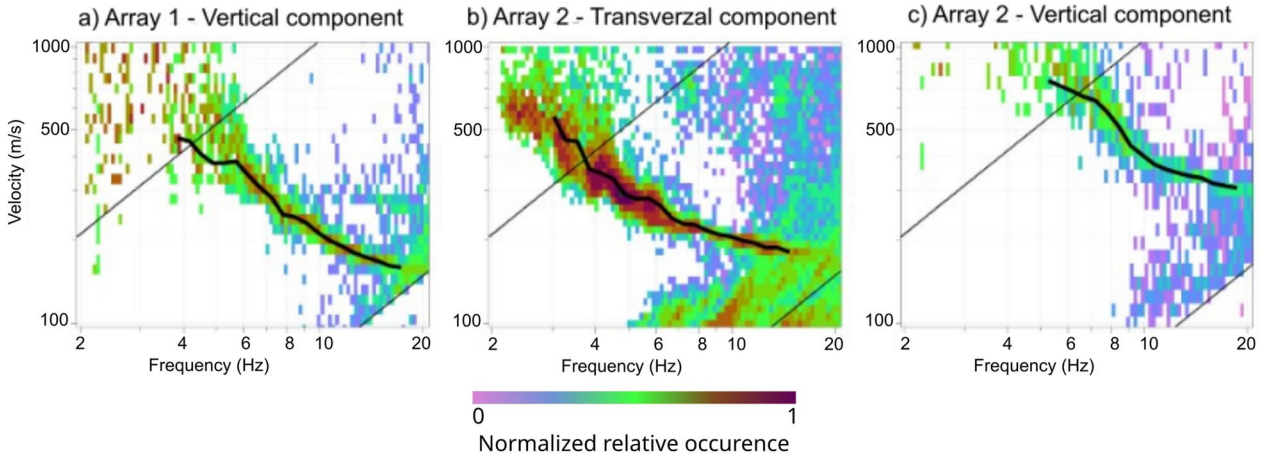

Fig. 2 Three-component high-resolution F–K (3C-HRFK) processing results for the vertical component of Array 1 (**a**), the transversal component of Array 1 (**b**), and the vertical component of Array 2 (**c**). They correspond to the histograms of the analysed time windows at the respective frequency ranges. Thin solid and dashed black lines are the array resolution limits. Thick solid black lines are selected from the data, where the central line indicates the best-fitted values obtained by fitting a Gaussian

Results

Array analysis

For creating the 3D velocity model, we estimated the seismic velocities at the selected site of the Mýtina maar using the array measurements. All Geopsy, Wavedec and ArrayTools3C codes were used for the estimation of the dispersion curves, resulting in a good agreement between the different estimates. The Wavedec dispersion curve was estimated in a narrower frequency band with respect to high-resolution methods. The results of three-component high-resolution F–K analysis estimated by ArrayTools3C code are shown in Fig. 2. Array 1, located on the lacustrine sediments, has yielded dispersion curves between 4 and 14 Hz of the fundamental mode of Love (L0) and Rayleigh (R0) waves (Fig. 2a, b, respectively). In contrast, for Array 2, located on the volcanic breccia, we were not able to determine the L0 dispersion curve, and we could only use the R0 between 5 and 15 Hz (Fig. 2 c).

Inversion of the dispersion curves was done using the Dinver module of the Geopsy software. The inverted profile was divided into layers with increasing thickness and range of S-wave velocities to be searched through. We forced increasing velocity with the depth option since we did not expect any low-velocity layers according to the borehole log. The resulting profile of the first array show increase in velocities, but no distinctive interface (Fig. 3c); however, the second array data results show an interface at 20 m depth due to significant step-like increase of S-wave velocity (Fig. 4b, Table 1). The velocity profile inversions resolution depth using dispersion data is usually related to a fraction of the maximum resolved wavelength in the phase velocity (λmax). For example, Cox and Teague (2016) proposed setting the resolution depth from λmax/3 to λmax/2. Considering the upper bound (λmax/2), the estimated resolution depths are 85 m and 75 m for Array 1 and Array 2, respectively. This is reasonable since the scatter of the inverted profiles starts to increase below these depths (Figs. 3, 4). The best fitting velocity profiles were then used for characterisation of the 80 m-deep lacustrine fill and the superficial S-wave velocity of the volcanic breccia.

Development of the 3D model

The development of elastic 3D models material parameters (P-wave velocity, S-wave velocity and density) of Mýtina maar was based on the density model in Mrlina et al. (2009). This model describes the near-surface geological parts of the maar. These include sedimentary fill lying on top of a volcanic breccia which is enveloped by an outer denser volcanic breccia, which has a similar density as a surrounding country bedrock (see Fig. 1).

Superficial S-wave velocities of the maar infills were well constrained by the array analysis in the top 80 m. Although the S-velocity is not well resolved below 80 m, we used the increase of the velocities observed in the inverted profile of Array 1 down to a depth of 200 m. Shear wave velocity of 1500 m/s was assumed as a maximum velocity of volcanic breccia and was kept constant below the depth of 200 m. For the country bedrock, we used values from regional tomography (Málek et al. 2005). The inverted velocity profile of Array 1 was used to simulate the lacustrine sediments, the profile based on Array 2 was then used for the breccia at the outside edges of the maar and in the depth also for the breccia under the lacustrine sediments. According to the gravimetric

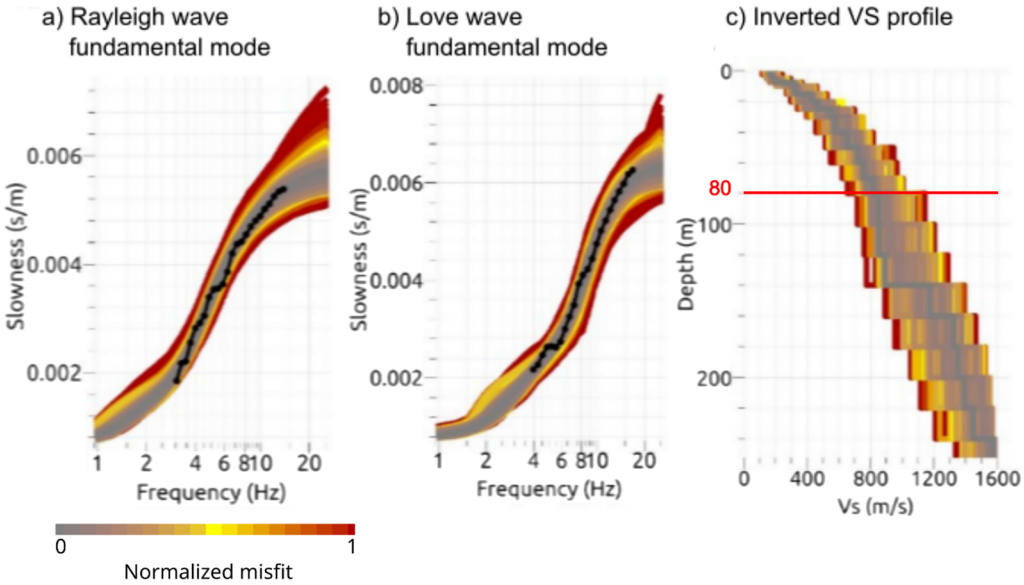

Fig. 3 Inversion results for Array 1, **a** Array 1—fundamental Rayleigh mode, **b** Array 1—fundamental Love mode, **c** Array 1—inverted Vs profile. Synthetic data from the inverted models are drawn using a colour scale. The depth of 80 m is the estimated resolution depth. Thick solid black dot-lines are the observed dispersion curves

survey (Mrlina et al. 2009), the inner breccia has lower density and presumably lower Vs velocity with respect to the outer breccia. Since we have velocity profiles estimated only for two locations (Array 1—central part of the maar; Array 2—outer part of the maar infill) and not for the inner breccia (transition zone from the centre to the edge of the maar), we used a horizontally averaged value for the inner breccia. The P-wave velocity was set so that Vp/Vs ratio equals square root of 3 for the whole model.

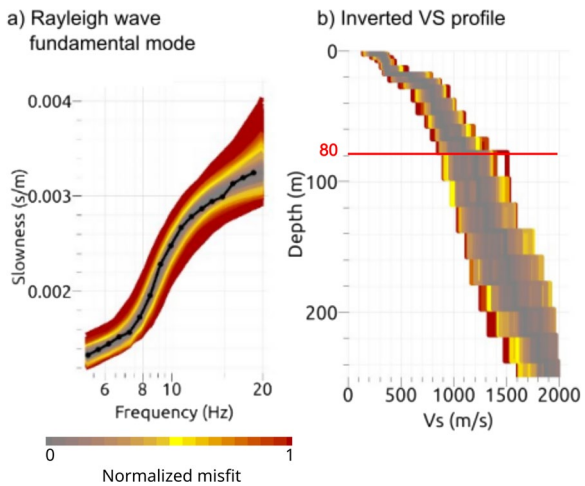

Fig. 4 Inversion results for Array 2, **a** Array 2—fundamental Rayleigh mode **b** Array 2—inverted Vs profile. Synthetic data from the inverted models are drawn using a colour scale. The depth of 80 m is the estimated resolution depth. Thick solid black dot-line is the observed dispersion curve

The modelling aimed to test different 3D velocity models and to determine the depth of the volcanic breccia, which could not be obtained from the inversion of a gravimetric survey (Mrlina et al. 2009) and the sensitivity of synthetic seismic noise modelling to the changing depth of the models.

The initial material model was a 3D vertical cone of a maar structure in the regional bedrock (Málek et al. 2005). To test the depth sensitivity, we also created a vertical cylindrical model representing an infinitely long cone. After setting the lateral dimensions of the cone and determining the depth, we added the sedimentary fill in the top centre of the cone and tested its influence on the ground motion amplification levels. According to Mrlina et al. (2009), we also added a transition zone of the outer breccia (see Fig. 5). As a next step, we likewise changed the shape to an elliptical cone to simulate different

Table 1 Shear wave velocities were obtained from array analysis. Array 1 corresponds to V_s sediments, Array 2 then to V_s outer breccia. V_s of the inner breccia in the first 100 m was set as a mean value between the two arrays

Depth (m)	V_s sediments (m/s)	V_s inner breccia (m/s)	V_s outer breccia (m/s)
0	166	193	221
20	256	312	369
40	564	668	772
60	625	764	903
80	741	947	1153

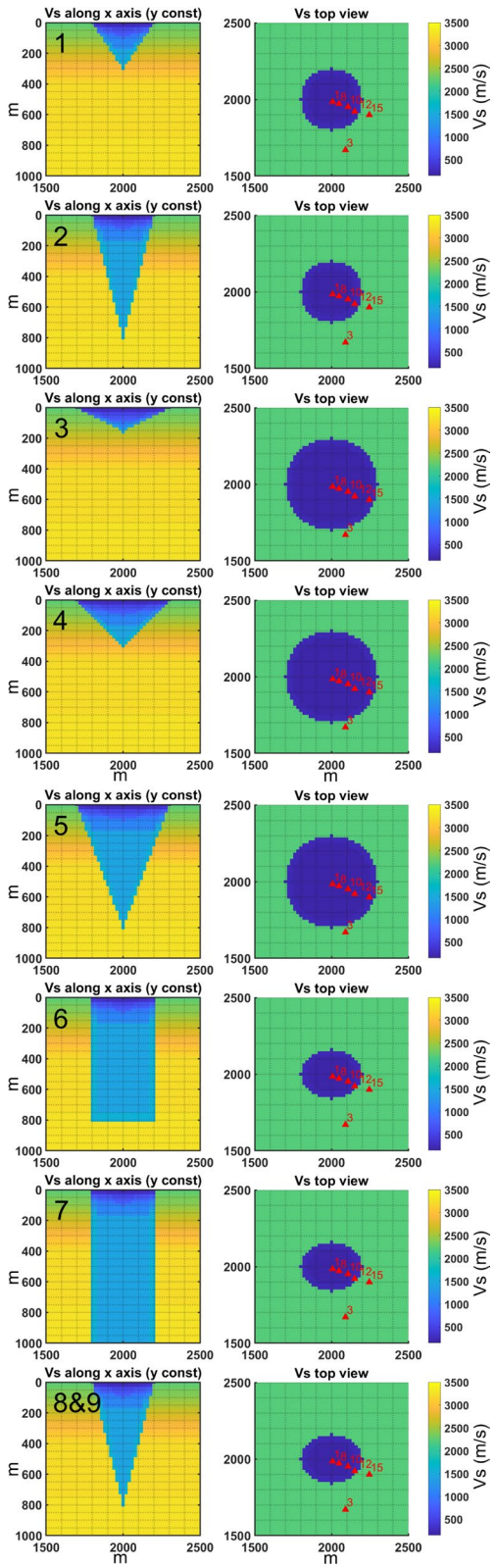

Fig. 5 Shear wave velocity models' cross-sections. Left side: vertical shear wave velocity cross-section, right side: horizontal view of shear wave velocity of Models 1 to 8, sorted like in Table 2. Viscoelastic Model 9 has the same shear wave velocity as Model 8, which is purely elastic

resonant frequencies in two perpendicular directions. Finally, we adopted a viscoelastic model described by quality factors Q_p and Q_p based on the empirical formulas of Campbell (2009). For Q_s, we used the relation $Q_s = 7.17 + 0.0276$*Vs, where Vs is seismic shear wave velocity in [m/s] at the depth, whilst $Q_p = 2 \cdot Q_s$.

Synthetic seismic noise analysis

The seismic noise simulation has been computed using the fourth-order finite differences code SW4 (Petersson and Sjorgreen 2015, 2017). The computational grid is 4×4×2 km with a horizontal and vertical spacing of 10 m with two refinement grids at 100 and 40 m in depth, each of them dividing the spacing to 5 and 2.5 m, respectively, and therefore keeping the requirement of at least 6 points per S-wave wavelength even for near-surface low-velocity layers.

The six selected stations (one located outside of the maar on the bedrock, and five stations in the maar aligned on a profile pointing from the centre of the maar to the edge) were adopted in the simulations. The seismic source is composed of independent body forces in three perpendicular directions and the displacement is registered in the same three directions for each of the forces resulting in nine computed components of the Green's tensor for each receiver. We created two grids of 92×92 virtual receivers (locations of the noise sources) at depths of 0 and 1 km. The virtual receiver grids are spaced by 30 m and are offset by 600 m from the horizontal edges of the computational grid to avoid entering inside the absorbing boundary. Two hours of noise synthetics were then generated by summation of responses to randomly distributed point-force sources, convolved with randomised source time functions as in Burjánek et al. (2019).

The synthetic seismograms were analysed by site-to-reference spectral ratio (SRSR), with the station outside of maar as a reference station. We computed Fourier spectra from 0.5 to 30 Hz of the seismograms. The spectra were then divided by the spectrum of the reference station outside of the maar, all for respective components. We searched the SRSR for the peak of the fundamental mode resonance frequency (automated search

Table 2 Models' geometry and resulting resonant frequencies and amplification levels: radius of sediments; thickness of sediments; radius of breccia; thickness of breccia; f_0^X, f_0^Y, f_0^Z the fundamental frequency at components X, Y, Z; A_0^X, A_0^Y, A_0^Z— amplification levels (SRSR) for the components X, Y, Z at the corresponding resonance frequencies (f_0^X, f_0^Y, f_0^Z). See Fig. 5 for the geometry of the models. Observed data marked with an abbreviation: obs

Model	Sediments rad. (m)	Sediments thick. (m)	Breccia rad. (m)	Breccia thick. (m)	f_0^X(Hz)	f_0^Y(Hz)	f_0^Z(Hz)	A_0^X	A_0^Y	A_0^Z
1	100	100	200	300	1.88	1.89	2.20	83	76	30
2	100	100	200	800	1.81	1.83	2.00	72	63	22
3	200	100	300	150	1.73	1.74	2.00	66	60	12
4	200	100	300	300	1.62	1.62	1.87	56	50	18
5	200	100	300	800	1.52	1.52	1.68	43	37	18
6	100	100	160–200	800	1.83	1.88	2.05	80	70	24
7	100	100	160–200	2000	1.82	1.87	2.04	78	60	24
8	100	100	160–200	800	1.85	1.91	2.10	82	70	30
9	100	100	160–200	800	1.85	1.91	2.10	35	31	20
obs					1.83	1.91	1.83	23	25	6

where the derivative of the curve is smaller than a set threshold for a certain number of values, starting the search from the lowest frequencies) and obtained the frequency and amplification level at that frequency. We compared these results with the observed data.

Several velocity models with an increasing level of complexity were tested. The sensitivity of the resulting resonance frequencies on the dimensions of the crater was explored. In addition, some of these models were further modified to fit the observed response. All models are listed in Table 2 and corresponding cross-sections of the 3D velocity models are shown in Fig. 5. Table 2 also shows modelled frequencies of the fundamental mode and corresponding amplification levels at station MYT001, which is situated right at the centre of the maar infill and the strongest amplification was observed at this station. All these models adopt lacustrine sediments, inner breccia and a transition zone 40 m wide of the outer breccia. The first five models shown are circular cones with various radii of sediments and breccia and differ in depth. Models 1 and 2 have depths of breccia cone set to 300 and 800 m to test sensitivity to the absolute depth of the crater. The difference in resonance frequency is most significant on the vertical component, but it is also present on the horizontal components. The amplification levels are lower on all components in case of the Model 2.

The next three Models—3, 4 and 5—have a longer radius of sedimentary fill and breccia by 100 m compared to Models 1 and 2 and are also tested for different maximum depths of breccia. The bigger diameter of the models results in decrease in both the resonance frequencies and the amplification levels, compared to Models 1, and 2.

Models 6 and 7 are elliptical cylinders with circular sedimentary fill and elliptical breccia structures. The major 200 m axis and the minor 160 m axis are set to test the splitting of the resonance frequency in two perpendicular horizontal directions, which is later observed in the data. Furthermore, the maximum depth of 2000 m for the breccia in Model 7 is set to study the possible depth sensitivity of the resonant frequencies. The results show that Models 6 and 7 differ only by 0.01 Hz at all components of the resonance frequency and only by a factor of 10 for the amplification ratio on the Y component. That is the fundamental frequency becomes insensitive to the maximum depth, and 2D resonance develops in case of Models 6 and 7.

The last two Models 8 and 9 are elliptical conical breccia structures with circular sedimentary fill and are the most complex ones. Model 8 is purely elastic, whereas Model 9 also adopts visco-elasticity characterised by quality factors Q_p and Q_s. The resonance frequency is the same in the case of both models, but the amplification level is strongly reduced (compare component in Figs. 6a and Fig. 7).

Comparison with the observed data

The comparison of modelled and observed spectral ratios for five site-to-reference station pairs are provided in Figs. 6 and 7. The recorded seismograms were systematically rotated around the vertical axis to decouple two perpendicular resonance modes observed on the horizontal components. In particular, SRSR were calculated for each of these directions and the optimum rotations were estimated. The observed data have a peak of fundamental mode resonance frequency at 1.91 Hz for the component rotated by 60 degrees clockwise from north (see Fig. 6b)

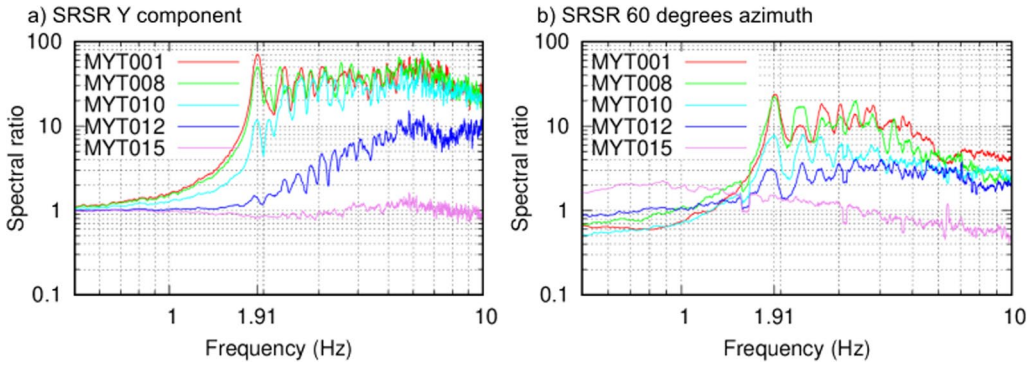

Fig. 6 Simulated and observed site-to-reference spectral ratios: **a** SRSR of the Y synthetic component for the elastic elliptical cone Model 8, **b** SRSR of the corresponding observed rotated data by 60 degrees clockwise from north

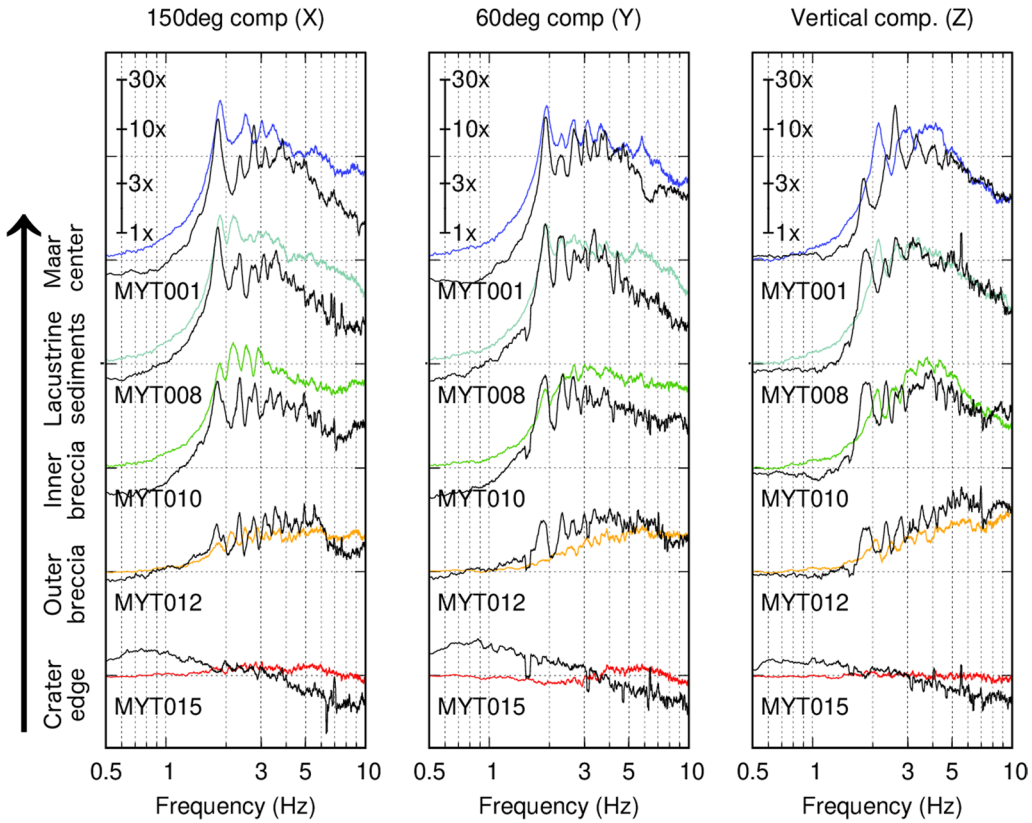

Fig. 7 Simulated and observed site-to-reference spectral ratios considering the viscoelastic Model 9 (colour) and observed data (black) for two horizontal components (150 degrees and 60 degrees) and the vertical component of ground motion. The order of the curves in the plots (from bottom to top) roughly follows the profile from the centre of the maar to its border

and 1.83 Hz for the component rotated by 150 degrees (Fig. 7). The vertical component varies between these two values, creating a wide peak (Fig. 7). The azimuth of 150 degrees is aligned with the slight elongation of the studied maar valley, which is also aligned in the same direction as TFZ (Flechsig et al. 2015), the azimuth of 60 degrees is then in agreement with the minor elliptical axis of the valley. Since we do not observe any preferential directions of motions at reference station MYR003 which is located just at the crater edge of the maar and within the TFZ, the observed directionality originates in the maar infills. The observed directions of N150 and N60 might result from the geometrical shape of the

crater, which could have been shaped by the lava effusions along the TFZ.

To simplify the modelling, we set the major and minor axis of the ellipse in the directions of the Cartesian coordinates X and Y of the computational domain, respectively. The observed data Cartesian system was rotated by 60 degrees to have the azimuth 60 and 150 degrees, which is in agreement with the TFZ (oriented about 150 degrees NW–SE).

A detailed comparison with the measured data is performed for the most complex Models 8 and 9, which show the best agreement with the observations. As we can see in Fig. 6, the synthetics generated for Model 8 agree with the observed data in terms of the resonance frequency of the fundamental mode, but the amplification level is much stronger in the case of synthetics. The resonance frequency is the same at all the stations, that is, the whole maar resonates as a whole body and exhibits a 3D local effect. Also, the modelled amplification decreases at the stations (MYT008 and MYT010) further from the centre of the maar (station MYT001), in agreement with the observed trend. Stations MYT012 and MYT015 located at the very edge of the maar fills, are showing a low peak in both cases, which demonstrates the possibility of mapping the lateral dimensions of the maar infills by ambient noise measurements.

Finally, the comparison with the observed response is done for the viscoelastic Model 9 (Fig. 7). The synthetic amplification curves show a better fit to observed amplification curves for elastic Model 8. For comparison, see Fig. 8, which shows the best fit for the Models 1–9. The frequency misfit was calculated using formula:

$$misfitF = |synf_0^x - obsf_0^x| + |synf_0^y - obsf_0^y| + |synf_0^z - obsf_0^z|,$$

where f_0^X, f_0^y, f_0^z are fundamental frequencies for the synthetic model (marked syn) and observed data (marked obs). The spectral ratio misfit was calculated using formula:

$$\begin{aligned} misfitA =& |log(synA_0^x) - log(obsA_0^x)| \\ &+ |\log(synA_0^y) - log(obsA_0^y)| \\ &+ |\log(synA_0^z) - log(obsA_0^z)|, \end{aligned}$$

where A_0^X, A_0^y, A_0^z are spectral ratios for the synthetic model (marked syn) and observed data (marked obs).

In the case of the horizontal components, both the resonance frequency and amplification level of the fundamental mode are better explained, and, on top of that, the level of high-frequency amplification is fitted as well. In the case of the vertical component, the synthetics still show a higher resonance frequency of 2.1 Hz than the observed data (see Fig. 7 and Table 2 for comparison between the models). All the tested conical and cylindrical models show the modelled vertical resonance is decoupled from the horizontal ones and the resonant frequency is generally higher for the vertical component, in contrast to the observations at Mýtina maar (Fig. 7). Comparisons with the observed data for all Models 1—8 are shown in Additional file 1: Fig. S2.

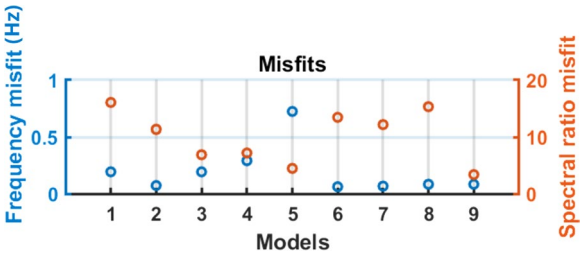

Fig. 8 Comparison between the models and observed data on the station MYT001. The blue circles show frequency misfit of all three components combined, the red circles show spectral ratio misfit of all three components combined

Discussion

Although the presented models are rather simple, they fit surprisingly well with the observed response and can be used as a proxy for the crater's estimated depth. Nevertheless, these models can hardly be considered as unique subsurface images of Mýtina maar. The simulated resonant frequencies and amplification levels depend on many parameters, and some of them are not well constrained. To make reliable depth estimates, it is necessary to constrain the seismic velocities of the crater infills (lacustrine sediments, breccia). Seismic velocities used to create the maar material parameter models in this study were set according to the array measurements valid only for the shallow subsurface down to the depths of 80 m. For the deeper parts of volcanic breccia, the value of 1500 m/s for the shear wave (S-wave) velocity was not constrained by any in situ data and was only assumed. However, it is in accordance with Gebhardt et al. (2011), who reported values of 2400 m/s for an acoustic wave (P-wave) in volcanoclastic breccia. Yet, the extrapolation of seismic velocity in breccia, as done in this study, might still cause a substantial error in the determination of the crater's depth.

The V_p/V_s ratio of the square root of 3 (1.73) was assumed for the entire model and was taken from the regional velocity model (Malek et al. 2005) for the seismically active zone of Nový Kostel, 25 km north of the Mýtina maar. Other V_p/V_s ratios were not tested, as we presumed low sensitivity of the resonant frequencies to the V_p velocity structure. It is likely, that the layer of the lacustrine sediments has a higher V_p/V_s due to high water saturation. Therefore, heterogeneous V_p/V_s ratios are

another complexity, which might be introduced to such modelling in future.

The lateral dimension of the crater's infill has also a strong influence on the results (resonant frequencies, amplification levels). Therefore, before even testing the model's sensitivity to the crater's depth, one should constrain the lateral dimensions by available geophysical measurements. This can be taken, for example, from a map of geomagnetic anomalies or dense ambient vibration measurements.

The results for cylindrical models (models 6 and 7) show that studied 3D resonance has a limiting threshold in sensitivity of depth determination. In particular, in case of deep craters with steep walls, 2D resonance develops and resonant frequencies do not depend on the absolute depth of the crater anymore. Therefore, a priori knowledge of the shape and structure of the studied crater should be considered, if available. It is illustrated in Fig. 8, where we observe the best frequency misfit between the models and the data at station MYT001 and synthetics of Models 6—9. The results are very similar regardless of geometry (cylindrical versus conical) and depth (Model 7 with depth of 2000 m, and Models 6, 8, 9 800 m). Added to that, models 6, 7 and 8 exhibit a very similar spectral ratio misfit. Nevertheless, Model 9, with identical dimensions and the velocity parameters as Model 8, has the best spectral ratio misfit due to the applied attenuation. Models 2, 6, 7 would have lower spectral ratio misfit comparable to Model 9 if the attenuation was considered in the modelling. At the station MYT012, placed within the outer breccia, we observe that the vertical component resonance frequency is not split from the horizontal ones, and that it is fitting the observed data best of all cases (Additional file 1: Fig. S2). This indicates that the boundary between the maar and the bedrock might be steeper and/or have more complicated shape (e.g. parabolical) than it is suggested in Models 8 and 9.

The modelled resonance was clearly decoupled on both horizontal and vertical components. The vertical component fundamental mode frequency was significantly higher with respect to the horizontal components. In contrast, such decoupling is not observed for the recorded ground motions at Mýtina maar. That is, the same resonant frequencies were observed for the vertical and horizontal components. This is quite a fundamental inconsistency, which might be addressed by more sophisticated models. For example, the models assumed in this study are rotationally symmetrical along the vertical axis (except the elliptical models). However, crater infills could be generally more complex, containing lateral inhomogeneities in form of volcanic veins, and layers of high-velocity volcanic rocks as shown, for example, by Závada et al. (2010) for Boren diatreme.

Conclusion

We propose a 3D model of the Mýtina maar comprising seismic velocities, density and attenuation. The model was used for simulating seismic wave propagation in the maar infills. The modelled seismic wavefield shows amplification of seismic waves inside the maar relative to the reference station outside in the bedrock. The amplification is split into two modes, this can be explained by the elliptical shape of the maar cone, where each half-axis corresponds to each resonance frequency. The surface lateral dimensions of the maar were selected from previous studies and field measurements, leaving the model unconstrained in the larger depths. Using the synthetic noise data, we demonstrate possibility of mapping the lateral dimensions of the maar infills by ambient noise measurements. From modelling, the depth of the maar breccia cone was determined to be around 800 m. The depth resolution is better for the initial cylindrical cone model, where the vertical resonance frequency has changed more significantly than for the elliptical cone. The subsurface sedimentary layer causes stronger ground motion amplification and a shift in the resonance frequency of the entire structure and cannot be neglected. The simulations based on perfectly elastic models overestimate the observed amplification levels, whilst seismic attenuation can limit the amplification levels to reasonable values.

Abbreviations

1D	One dimensional
3D	Three dimensional
A/D	Analogue-to-digital
ERT	Electric resistivity tomography
F–K	Frequency wavenumber
GPS	Global positioning system
L0	Love wave fundamental mode
NW	North west
P-wave	Primary wave
Qp	Attenuation factor of P-wave
Qs	Attenuation factor of S-wave
R0	Rayleigh wave fundamental mode
SE	South-east
SRSR	Site-to-reference spectral ratio
SST	Shallow seismic tomography
S-wave	Shear wave
TFZ	Tachov fault zone
Vp	P-wave velocity
Vp/Vs	Ratio between P-wave velocity and S-wave velocity
Vs	S-wave velocity

Supplementary Information

The online version contains supplementary material available at https://doi.org/10.1186/s40623-023-01822-7.

Additional file 1. Figure S1. H/V spectral ratio of the reference station. Left—E component, right—N component. Figure S2. Simulated and observed site-to-reference spectral ratios for models 1-8.

Acknowledgements
We would like to thank Shinichi Matsushima, Marta Pischiutta and anonymous reviewer for constructive comments and helpful reviews. We also thank Anders Petersson and Björn Sjögreen for making their FD code SW4 available. This work was supported by Czech Science Foundation (GACR), project no. GA20-15818S, and by the Ministry of Education, Youth and Sports of the Czech Republic through the e-INFRA CZ (ID:90140).

Author contributions
ML is involved in field experiments, interpreting the data, numerical modelling and writing. IO is involved in numerical modelling, writing and draft corrections. JB is involved in conceptualisation, field experiments, data interpretation, writing, draft corrections and supervision. All authors read and approved the final manuscript.

Funding
This study was supported by Czech Science Foundation (GACR), project no. GA20-15818S; Ministry of Education, Youth and Sports of the Czech Republic, e-INFRA CZ (ID:90140).

Availability of data and materials
The data analysed in this paper were gathered in the framework of a Ph.D. project. The data, models and synthetics are stored at the Institute of Geophysics of the Czech Academy of Science and are available by request. Contact: Jan Burjánek (burjanek@ig.cas.cz).

Declarations

Ethics approval and consent to participate
Not applicable.

Consent for publication
Not applicable.

Competing interests
The authors declare that they have no competing interests.

Author details
[1]Institute of Geophysics of the Czech Academy of Science, Bocni II/1401, 141 00 Prague 4, Czech Republic. [2]Department of Geophysics, Faculty of Mathematics and Physics, Charles University, Prague, Czechia. [3]Institute of Technology and Business, Ceske Budejovice, Czechia.

Received: 6 October 2022 Accepted: 14 April 2023
Published online: 12 May 2023

References

Bonnefoy-Claudet S, Cotton F, Bard PY (2006) The nature of noise wavefield and its applications for site effects studies: a literature review. Earth-Sci Rev 79(3–4):205–227. https://doi.org/10.1016/j.earscirev.2006.07.004
Borcherdt RD (1970) Effects of local geology on ground motion near San Francisco Bay. Bull Seismol Soc Am 60(1):29–61. https://doi.org/10.1785/BSSA0600010029
Burjánek J, Kleinbrod U, Fäh D (2019) Modelling the seismic response of unstable rock mass with deep compliant fractures. J Geophys Res Solid Earth 124(12):13039–13059. https://doi.org/10.1029/2019JB018607
Campbell KW (2009) Estimates of Shear-Wave Q and K0 for unconsolidated and semiconsolidated sediments in Eastern North America. Bull Seismol Soc Am 99(4):2365–2392. https://doi.org/10.1785/0120080116
Capon J (1969) High-resolution frequency-wavenumber spectrum analysis. Proc IEEE 57:1408–1418. https://doi.org/10.1109/PROC.1969.7278
Cox BR, Teague DP (2016) Layering ratios: a systematic approach to the inversion of surface wave data in the absence of *a priori* information. Geophys J Int 207(1):422–438. https://doi.org/10.1093/gji/ggw282
Eisner L, Clayton R (2001) A reciprocity method for multiple-source simulations. Bull Seismol Soc Am 91(3):553–560. https://doi.org/10.1785/012000222
Fiala J, Vejnar Z (1997) The Cheb-Dylen Crystalline Unit, relations to the Moldanubian Zone. In: Vrána S, Štědrá V (eds) (1997) Geological model of western Bohemia related to the KTB borehole in Germany, 1st edn., Czech Geological Survey, Prague, ISSN 05819172, pp 56–57.
Flechsig C, Heinicke J, Mrlina J, Kämpf H, Nickschick T, Schmidt A, Seidl M (2015) Integrated geophysical and geological methods to investigate the inner and outer structures of the Quaternary Mýtina maar (W-Bohemia, Czech Republic). Int J Earth Sci 104(8):2087–2105. https://doi.org/10.1007/s00531-014-1136-0
Gebhardt AC, De Batist M, Niessen F, Anselmetti FS, Ariztegui D, Haberzettl T, Kopsch C, Ohlendorf C, Zolitschka B (2011) Deciphering Lake and maar geometries from seismic refraction and reflection surveys in Laguna Potrok Aike (southern Patagonia, Argentina). J Volcanol Geotherm Res 201(1–4):357–363. https://doi.org/10.1016/j.jvolgeores.2010.12.019
Irikura K, Kawanaka T (1980) Characteristics of microtremors on ground with discontinuous undergone structure. Bull Disas Prev Res Inst 30(3):81–96
Kleinbrod U, Burjánek J, Fäh D (2017a) On the seismic response of instable rock slopes based on ambient vibration recordings. Earth Planets Space. https://doi.org/10.1186/s40623-017-0712-5
Málek J, Horálek J, Janský J (2005) One-dimensional qP-wave velocity model of the upper crust for the West Bohemia/Vogtland Earthquake swarm region. Stud Geophys Geod 49(4):501–524. https://doi.org/10.1007/s11200-005-0024-2
Maranò S, Reller C, Loeliger H-A, Fäh D (2012) Seismic waves estimation and wavefield decomposition: application to ambient vibrations. Geophys J Int 191(1):175–188. https://doi.org/10.1111/j.1365-246X.2012.05593.x
Maranò S, Hobiger M, Fäh D (2017) Retrieval of Rayleigh wave ellipticity from ambient vibration recordings. Geophys J Int 209:334–352. https://doi.org/10.1093/gji/ggx014
Mrlina J, Kämpf H, Geissler W, van den Bogaard P (2007) Assumed Quaternary maar structure at the Czech/German border between Mytina and Neualbenreuth (western Eger Rift, Central Europe): geophysical, petrochemical and geochronological indications. Z Geol Wiss 35(4):213–230. https://doi.org/10.3989/mc.2004.v54.i276.257
Mrlina J, Kämpf H, Kroner C, Mingram J, Stebich M, Brauer A, Seidl M (2009) Discovery of the first Quaternary maar in the Bohemian Massif, Central Europe, based on combined geophysical and geological surveys. J Volcanol Geotherm Res 182(1–2):97–112. https://doi.org/10.1016/j.jvolgeores.2009.01.027
Petersson NA, Sjögreen B (2015) Wave propagation in anisotropic elastic materials and curvilinear coordinates using a summation-by-parts finite difference method. J Comput Phys 299:820–841. https://doi.org/10.1016/j.jcp.2015.07.023
Petersson NA, Sjögreen B (2017) SW4, version 2.01 [software]. Comput Infrastr Geodyn. https://zenodo.org/record/1063644. Accessed 2 Mar 2023.
Pischiutta M, Fondriest M, Demurtas M, Magnoni F, Di Toro G, Rovelli A (2017) Structural control on the directional amplification of seismic noise (Campo Imperatore, central Italy). Earth Planet Sci Lett 471:10–18. https://doi.org/10.1016/j.epsl.2017.04.017
Poggi V, Fäh D (2010) Estimating Rayleigh wave particle motion from three-component array analysis of ambient vibrations. Geophys J Int 180:251–267. https://doi.org/10.1111/j.1365-246X.2009.04402.x
Prieto GA, Parker RL, Vernon FL (2009) A Fortran 90 library for multitaper spectrum analysis. Comp Geosc 35:1701–1710. https://doi.org/10.1016/j.cageo.2008.06.007
Sambridge M (1999) Geophysical inversion with a neighbourhood algorithm—I. Searching a parameter space. Geophys J Int 138:479–494. https://doi.org/10.1046/j.1365-246X.1999.00876.x
Tonica J, Opletal M, Cicha I, Cihelka M (1998) Geologická Mapa ČR, Český geologický ústav, Praha (**in Czech**).
Wathelet M (2008) An improved neighborhood algorithm: parameter conditions and dynamic scaling. Geophys Res Lett. https://doi.org/10.1029/2008GL033256

Wathelet M, Jongmans D, Ohrnberger M, Bonnefoy-Claudet S (2008) Array performances for ambient vibrations on a shallow structure and consequences over Vs inversion. J Seism 12:1–19. https://doi.org/10.1007/s10950-007-9067-x

Wathelet M, Guillier B, Roux P, Cornou C, Ohrnberger M (2018) Rayleigh wave three-component beamforming: signed ellipticity assessment from high-resolution frequency-wavenumber processing of ambient vibration arrays. Geophys J Int 215(1):507–523. https://doi.org/10.1093/gji/ggy286

Wathelet M, Chatelain JL, Cornou C, Di Giulio G, Guillier B, Ohrnberger M, Savvaidis A (2020) Geopsy: a user-friendly open-source tool set for ambient vibration processing. Seismol Res Lett 91(3):1878–1889. https://doi.org/10.1785/0220190360

Závada P, Dědeček P, Mach K, Lexa O, Potužák M (2010) Emplacement dynamics of phonolite magma into maar-diatreme structures—correlation of field, thermal modeling and AMS analogue modeling data. J Volcanol Geotherm Res 201(1–4):210–226. https://doi.org/10.1016/j.jvolgeores.2010.07.012

Publisher's Note